applied optics

Numerical study on the scattering property of porous polymer structures via supercritical CO_2 microcellular foaming

Shudong Yu,[1] Jiadong Yu,[1] Junchi Chen,[2] Xinrui Ding,[1] Jiasheng Li,[1,3] Longshi Rao,[4] Yong Tang,[1] and Zongtao Li[1,3,*]

[1]National and Local Joint Engineering Research Center of Semiconductor Display and Optical Communication Devices, South China University of Technology (SCUT), Guangzhou 510640, China
[2]Light Technology Institute, Karlsruhe Institute of Technology (KIT), Engesserstrasse 13, Karlsruhe 76131, Germany
[3]Research and Development Center, Foshan Nationstar Optoelectronics Company Ltd., Foshan 528000, China
[4]College of Engineering, Shantou University, Shantou 515063, China
*Corresponding author: meztli@scut.edu.cn

Received 25 February 2020; revised 12 April 2020; accepted 14 April 2020; posted 15 April 2020 (Doc. ID 391449); published 8 May 2020

Disordered porous polymer structures have gained tremendous attention due to their wide applications in various fields. As a simple yet versatile technique, supercritical CO_2 microcellular foaming has been proposed to fabricate highly scattering porous polymer films, which have been used to enhance the efficiency of quantum dots (QDs) films. In the foaming process, numerous enclosed pores are generated, which induce significant scattering, underpinning the efficiency enhancement in optoelectronic devices. However, the scattering property of foamed porous structures has still not been well investigated, and effective guidelines for engineering the porous structures are still not available. In this work, we use Mie scattering theory and ray-tracing simulation to analyze the optical property of a single pore, pore assembly, and porous film. Furthermore, it is demonstrated that the scattering scheme in the porous QD films leads to a large enhancement of excitation light absorption and QD emission extraction. It is envisioned that our work will contribute to the engineering guidelines of porous structures and boost the application of porous structures in similar fields.

https://doi.org/10.1364/AO.391449

1. INTRODUCTION

Disordered structures with a broadband and strong scattering performance have gained tremendous attraction from academia and industry, due to their wide applications in traditional and emerging fields, such as wall painting [1], radiative cooling [2–4], solar cells [5], and light-emitting diodes (LEDs) [6,7]. To achieve a large scattering strength, materials with a large refractive index are usually adopted, among which titanium dioxide (TiO_2, $n \approx 2.6$) nanoparticles are the most commonly used pigment. It is well noted that the toxicity of TiO_2 nanoparticles has raised great concerns among researchers, which actively calls for particle-free scattering systems as an alternative, namely, porous polymer structures [8,9]. However, the scattering performance of porous polymers is usually not as good as that of TiO_2-based scattering systems, stemming from the low refractive index ($n \approx 1.5$) of polymers. Therefore, obtaining a prominent scattering performance based on porous polymers is of paramount importance to enable real-world applications. Intriguingly, many biological systems consisting of biopolymer exhibit highly scattering characteristics, thereby providing us natural models to mimic [10–12]. The best-known example is *Cyphochilus* spp., whose white scale is demonstrated to have the largest scattering strength among low-index scattering systems in nature [13]. The scale, with a thickness of 7 μm, reflects up to 70% of incoming light, outperforming many artificial scattering systems [14,15]. Further investigations have demonstrated that the outstanding scattering performance of the white beetle scale originates from its complex porous chitin structures with optimized filament size, filament filling fraction, and a certain degree of structure anisotropy [13–15].

Until now, numerous researchers have been focused on the biomimetic and bioinspired fabrication of highly scattering polymer structures. The first adopted technique is electrospinning, via which highly scattering porous nanofibers films are fabricated [16]. Note that such porous nanofibers films have been used in LED lamps to extract and control light emission from LED chips [17,18]. In addition, nonsolvent-induced phase separation was demonstrated to enable high filling fraction and anisotropy of porous structures, endowing the porous

films with remarkable scattering ability even better than that of the *Cychochilus* scale [19,20]. Moreover, the phase-separated polymer films were demonstrated as good radiative cooling materials [3] and light outcoupling layers in organic LEDs [21]. Additionally, researchers have directly engineered biopolymers (e.g., cellulose) into highly porous materials by the template method or the evaporation-induced technique [9,22], which were also an effective radiative cooling material for buildings [2]and light in-coupling layer for solar cells [23].

In recent years, a simple yet versatile technique, namely, supercritical CO_2 microcellular foaming, has been proposed to fabricate highly scattering porous polymer structures [8,24]. This technique was first used by Syurik *et al*. to generate densely packed pores in polymer films for obtaining efficiently scattering structures [8], and was later adapted by the same group to fabricate porous polymer matrix for quantum dots (QDs) encapsulation [24]. A significant increase factor of ~7 times in the photoluminescence (PL) intensity of QDs film by foamed porous structures was demonstrated, stemming from an increase of excitation light absorption and QD emission outcoupling. Though the application feasibility of the foamed porous structures have been demonstrated, the scattering mechanism of such porous polymer systems is still not fully understood, and guidelines for engineering porous structures in specific application fields are still not available. In this paper, we target a porous polymer system fabricated by supercritical CO_2 microcellular foaming [24] and systematically study the scattering property based on numerical models. As a proof of concept, the scattering-enhanced QD system is exemplified. Our study reveals the optical mechanism underpinning the PL enhancement in porous QD films and generates some guidelines for engineering a porous scattering medium.

2. METHODS

A. Microcellular Foaming by Supercritical CO_2

Supercritical CO_2 microcellular foaming is a well-established process utilized to enhance the mechanical, thermal and optical properties of polymer by introducing numerous pores inside. The microcellular process consists of four steps: (i) polymethyl methacrylate (PMMA) is used as the foamed matrix because PMMA is amorphous and CO_2-philic and is also a common QD encapsulation medium with high transparency in the visible range. As shown in Fig. 1, PMMA samples are put into a high-temperature autoclave (applied temperature T: 25–90°C) under a high-pressure environment filled with CO_2 (applied pressure P: 4–50 MPa); (ii) with applied temperature and pressure higher than the critical values of CO_2 (31°C, 7.38 MPa), CO_2 is turned into a supercritical and starts to dissolve into a PMMA matrix, forming a homogeneous PMMA/CO_2 system in the saturation state. Note that the dissolved CO_2 decreases the glass transition temperature T_g of PMMA, well known as the plasticization effect; (iii) with a pressure-quenching or temperature-rising operation, the formed PMMA/CO_2 becomes supersaturated with small-sized pores nucleating; (iv) the nucleated pores grow into larger ones with CO_2 continuously diffusing until $T < T_g$. More details about the foaming process can be referred to in a previous publication [24].

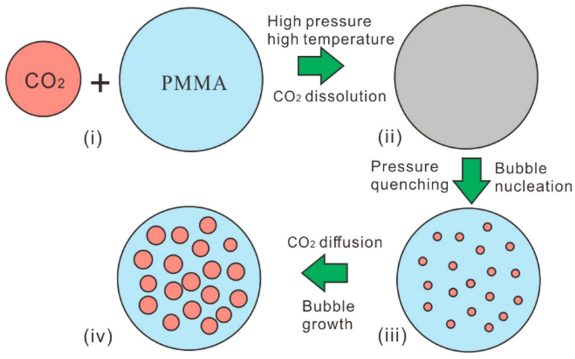

Fig. 1. Schematic diagram of microcellular foaming based on supercritical CO_2.

The introduced pores in the PMMA matrix induce significant scattering, which is related to the geometric parameters of pores, including pore size, number density, shape, and arrangement mode. Pore shape and arrangement are difficult to change in the foaming process, whereas pore size and number density are easier to tune. Therefore, we can engineer the optical property of the foamed porous polymer by tailoring the pore size and number density. In the proposed foaming process, three parameters, including foaming pressure, temperature, and molecular weight of PMMA are varied to induce different pore morphology, namely, different pore size and number density. By combining the foaming pressure, temperature, and PMMA molecular weight in a pressure-quenching-initiated foaming process, one can tune the pore size from tens of nanometers to several micrometers in diameter. Note that the pore number density is related to the volumetric filling fraction of pores. With the filling fraction ranging from ~5% to ~50% confirmed in the experiments, one can calculate the pore number density for a certain pore size.

Prior to the optical modeling, we should first analyze the pore morphology of foamed PMMA film. Under the foaming condition of 50 MPa at 80°C, PMMA film with a pristine thickness of 7 μm coated on a glass substrate was successfully foamed. The cross-sectional morphology of the porous PMMA film is obtained by using scanning electron microscopy (SEM) as shown in Fig. 2. It is observed that the sample contains a planar skin layer and a pore layer, in which pores show a spherical shape and are well separated by a thin polymer wall. From an optical aspect, we can treat the pores as ideal spheres in the modeling and analyze the scattering property of a single pore, then of pore assembly, and lastly, of porous films.

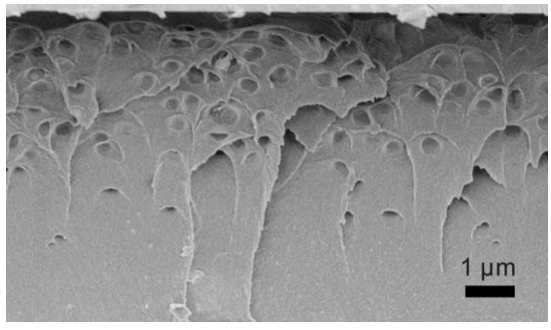

Fig. 2. SEM image of cross section of foamed PMMA film with nanosized pores.

B. Mie Scattering Modeling

Since the pores show a spherical shape, it is reasonable to use Mie scattering theory for modeling the pore and studying pores' scattering property [25]. Following is the brief introduction of Mie scattering theory and related parameters needed for calculation.

Pore scattering can induce the variation of the impinging light polarization. To describe this phenomenon, we can resolve the polarization into components parallel and perpendicular to the scattering plane and relate the scattering ($E_{\parallel,\mathrm{sca}}$, $E_{\perp,\mathrm{sca}}$) and incident fields ($E_{\parallel,\mathrm{inc}}$, $E_{\perp,\mathrm{inc}}$) through

$$\begin{pmatrix} E_{\parallel,\mathrm{sca}} \\ E_{\perp,\mathrm{sca}} \end{pmatrix} = \frac{e^{ikr}}{kr} \begin{pmatrix} S_2 & S_3 \\ S_4 & S_1 \end{pmatrix} \begin{pmatrix} E_{11,\mathrm{inc}} \\ E_{\perp,\mathrm{inc}} \end{pmatrix}, \tag{1}$$

which defines the amplitude scattering matrix and where r is the distance from observation position to the pore, k is the wavenumber ($k = 2\pi/\lambda$, λ is the light wavelength), $S_3 = S_4 = 0$ for a spherical pore, and in terms of scattering angle θ, S_1, and S_2 can expressed as

$$S_1(\theta) = \sum_{n=1}^{\infty} \frac{2n+1}{n(n+1)} [a_n \pi_n + b_n r_n], \tag{2}$$

$$S_2(\theta) = \sum_{n=1}^{\infty} \frac{2n+1}{n(n+1)} [a_n \tau_n + b_n \pi_n], \tag{3}$$

where a_n and b_n are the expansion coefficients with even symmetry and odd symmetry, respectively. a_n and b_n are calculated by

$$a_n = \frac{m\psi_n(mx)\psi_n'(x) - \psi_n'(mx)\psi_n(x)}{m\psi_n(mx)\xi_n'(x) - \psi_n'(mx)\xi_n(x)}, \tag{4}$$

$$b_n = \frac{\psi_n(mx)\psi_n'(x) - m\psi_n'(mx)\psi_n(x)}{\psi_n(mx)\xi_n'(x) - m\psi_n'(mx)\xi_n(x)}, \tag{5}$$

where x is the size parameter ($x = kR$, R is the pore radius), m is the relative refractive index of pores, and $\psi_n(x)$ and $\xi_n(x)$ are the Riccati–Bessel functions.

C_{sca} and Q_{sca} are the scattering cross section and scattering efficiency, respectively, which can be calculated by using the formulas above,

$$C_{\mathrm{sca}} = \frac{2\pi}{k^2} \sum_{n=1}^{\infty} (2n+1) \left(|a_n|^2 + |b_n|^2 \right), \tag{6}$$

$$Q_{\mathrm{sca}} = \frac{2\pi}{x^2} \sum_{n=1}^{\infty} (2n+1) \left(|a_n|^2 + |b_n|^2 \right). \tag{7}$$

Further, according to Mie theory, the scattering coefficient μ_{sca} and asymmetry parameter g can be described as

$$\mu_{\mathrm{sca}} = NC_{\mathrm{sca}}, \tag{8}$$

$$g = \langle \cos\theta \rangle = \frac{1}{4\pi} \int_0^{2\pi} \int_0^{\pi} p(\theta, \varphi) \cos\theta \sin\theta \, d\theta \, d\varphi, \tag{9}$$

where N is the number density of pores and g is defined as the average of $\cos\theta$ weighting the contribution of each θ according to the angular distribution of normalized phase function $p(\theta, \varphi)$. $p(\theta, \varphi)$ is denoted as

$$p(\theta, \varphi) = \frac{4\pi F(\theta, \varphi)}{k^2 C_{\mathrm{sca}}}, \tag{10}$$

where $F(\theta, \varphi)$ is a dimensionless scattering function, which is obtained by the scattering amplitude functions $S_1(\theta)$ and $S_2(\theta)$.

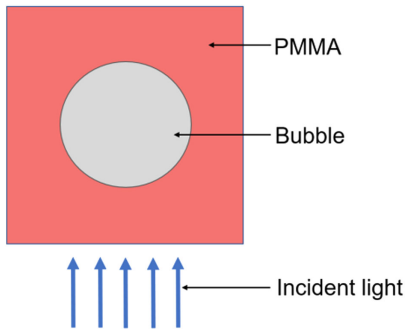

Fig. 3. Scattering model of a single spherical pore, consisting of incident light, PMMA medium, and spherical pore.

Figure 3 shows the optical model for Mie scattering analysis. It is seen that a single spherical pore is considered, and the surrounding medium is PMMA with a refractive index of 1.49. Note that the pore is made up of air, and there is no absorption for the pores. The optical parameters of the single pore were calculated based on this model, and for pores assembly, linear superposition was used without accounting for the interactive scattering phenomenon.

C. Monte Carlo Ray Tracing

The Monte Carlo algorithm was used for the ray tracing of the porous film model. Specifically, the commercial ray-tracing software, Tracepro, was used for the simulation. Pores were treated as the Mie scattering centers in the model. The scattering coefficient μ_{sca} obtained in Eq. (8) was used as an input parameter in the ray-tracing model. Since the simulation model cannot calculate the propagation of light scattered by the pores, we use the Henyey–Greenstein function to approximate the generation of the angular scattering [26]. This function is expressed as

$$p(\theta) = \frac{1 - g^2}{4\pi \left(1 - 2g\cos\theta + g^2\right)^{3/2}}, \tag{11}$$

where g is the asymmetry parameter obtained in Eq. (9). The g ranges from -1 to 1. When $g = -1$, all light is scattered into 180°. When $g = 1$, all the scattered light is directed to 0°. Additionally, forward scattering is dominant when $0 < g < 1$, whereas backward scattering dominates when $-1 < g < 0$.

For simulating the QD emission, a fluorescence model was introduced in the simulation. The ray tracing of the fluorescence process consists of two steps: the first is the ray-tracing process of the excitation light, and the second is the ray tracing of the QD emission light. In the model, 405 nm light is used as the excitation light, while 545 nm light is adopted as the QD emission. The absorption coefficient and PL quantum yield of QD film

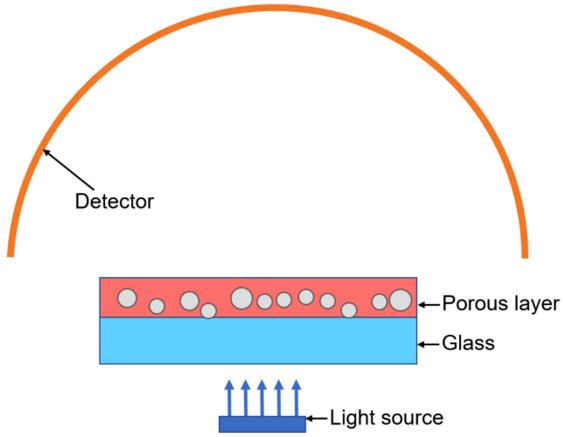

Fig. 4. Optical model of porous film for ray tracing, which includes a light source, a porous film (consisting of glass substrate and porous layer), and a detector.

are two important input parameters in the model, which were obtained from experimental measurement.

Figure 4 shows the optical model for ray tracing, which consists of a light source (parallel light), a porous film, and a detector. The porous film comprises a glass substrate (refractive index, 1.5) and a porous layer. The ratio between light power collected by the detector and incident light power was calculated as the total transmittance of porous films in the simulation. For the simulation, the blue light and PL powers exiting from six planes of the film, including two front surfaces and four edge surfaces, were collected and analyzed, respectively. The total PL power was obtained by summing up all the obtained PL powers exiting from six surfaces. In the display application, the PL emission exiting from the edge surface is usually not collected and is converted into wasted thermal energy [27], which accounts for a large ratio in the total QD emission for unstructured QD films [24]. To evaluate the influence of porous structures on the extraction of QD emission into front free space, here we define the ratio between the PL power exiting from two front surfaces and total PL power as the light extraction ratio of QD emission. In addition, the absorption of incident light power in the PMMA matrix was directly collected, since an absorption coefficient originating from QDs was assigned to the PMMA in the simulation model.

D. Characterization Methods

In this work, the cross-sectional morphology of porous films made by supercritical CO_2 was examined by SEM (Zeiss, SUPRA 55 VP). Prior to the observation, the films were immersed into liquid nitrogen and then directly fractured across the central position to expose the cross-sectional surfaces, which were then coated with a thin-film gold layer via sputtering to eliminate a charge effect during the observation process.

For optical characterization, we used a UV-Vis spectrometer attached with a 150 mm integrating sphere (PerkinElmer Lambda 1050) to measure the total transmittance (including ballistic and diffuse transmittance) over the 400–700 nm spectra. Additionally, a UV–Vis spectrometer (Agilent Cary 5000) integrated with a universal measurement accessory was used to obtain the angular transmitted light intensity with 650 nm light normally impinging on the porous films.

3. RESULTS AND DISCUSSION

A. Scattering Analysis of Single Pore

Based on Mie scattering theory, the scattering intensity is related to the polarization of incident light. Therefore, we first analyze the scattering intensity distributions of spherical pores with different radii under perpendicular and parallel polarized incident light. Accounting for the scattering symmetry from spherical pores, scattering intensity distributions are shown in the angle range 0–180°C, where 0–90°C denotes the forward scattering and 90–180°C represents the backward scattering. Under the 450 nm incident light, the scattering distributions generating from four kinds of spherical pores with different diameters (D = 50 nm, 500 nm, 5 μm, 10 μm) are shown in Fig. 5. It is seen from Fig. 5(a) that the scattering distributions stemming from small pores ($D = 50$ nm) for perpendicular and parallel polarized incident light differ greatly. Indeed, the scattering pattern is similar to the emission of a simple dipole. For perpendicular polarization, the scattering intensity is nearly unchanged with respect to scattering angle θ, while the intensity shows a variation of $\cos^2\theta$ for parallel polarization. With the increasing of pore size, the scattering intensity difference caused by the polarization is reduced. Meanwhile, the lobe number in the intensity curve increases, and the peak becomes sharp, which indicates a dominant forward scattering.

Figure 6 shows the scattering cross section and scattering efficiency of a single spherical pore with different diameters under three typical wavelengths (450, 550, and 650 nm). It is shown that the scattering cross section increases with the increasing pore size, since the scattering property of pores depends on the geometrical size [28]. When the pore size is far smaller than the incident light wavelength, the scattering property is mainly dependent on the pore volume. The scattering property of pores with much larger size than the wavelength mainly depends on

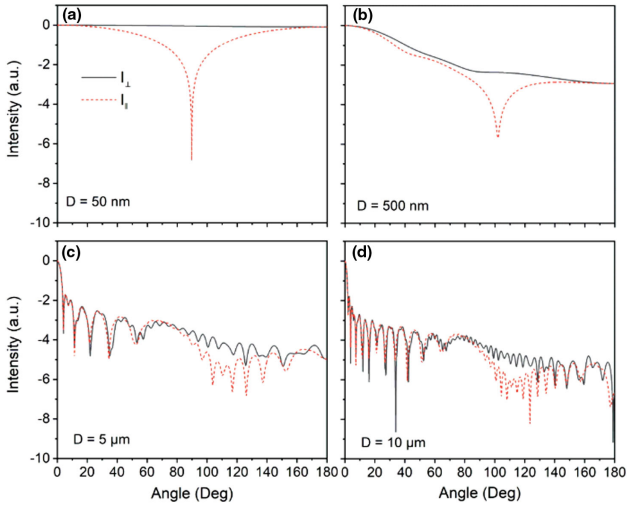

Fig. 5. Angle-dependent scattering intensity diagrams describing perpendicular and parallel polarized light scattered by spherical pores with different diameters (incident light wavelength, 450 nm). (a) 50 nm, (b) 500 nm, (c) 5 μm, and (d) 10 μm.

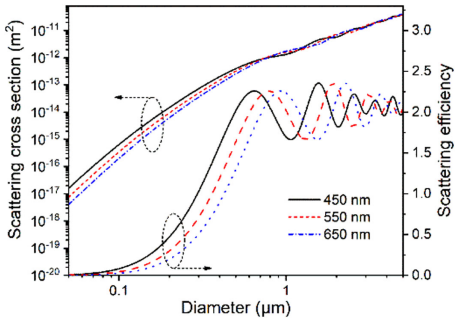

Fig. 6. Scattering cross section and scattering efficiency of a single spherical pore with different diameters embedded in PMMA medium (incident light, unpolarized plane waves with three wavelengths of 450, 550, and 650 nm).

the projected area of pores along the incident light direction. Such a scheme confirms the phenomenon that the scattering cross section of pores varies more dramatically with the size in the small size range, indicating that larger cross section variation is caused with unit diameter change. For example, the scattering cross section at $D = 500$ nm is 6.34×10^4 times that at $D = 50$ nm; note that the size changing factor is 10 times. While the size changes from 500 nm to 5 μm with the same size changing factor of 10, the scattering cross section increases only by 1.62×10^2 times. As regards different incident light wavelengths, it is demonstrated that a submicrometer-scale pore shows an evident wavelength-dependent scattering property and scatters short-wavelength light more efficiently (blue > green > red). This phenomenon becomes more evident when the pore size gets much smaller than the wavelength. In this size range, the scattering pattern is similar to that of Rayleigh scattering, in which the scattering intensity is inversely proportional to the fourth power of wavelength. Further, we examine the influence of pore size and incident light wavelength on the scattering efficiency. When the pore diameter is below 100 nm, the scattering efficiency has no obvious change with the increasing size. Above 100 nm, the scattering efficiency increases rapidly with the increasing pore size and attains the peak at $D = \sim 1$ μm, followed by asymptotically varying to a constant with a decaying oscillation. It has been demonstrated that the oscillations are caused by interference between near forward transmission and diffraction [29]. A larger scattering efficiency at short-wavelength incident light for submicrometer-scale pores also confirms the stronger scattering ability at the blue-light region.

To describe the spatial scattering distribution characteristics of pores well, several types of pores with different diameters ($D = 50$ nm, 250 nm, 500 nm, 1 μm, 2 μm, 5 μm) are selected for calculating their scattering phase distributions (SPDs), which are shown in Fig. 7. It is shown that the SPD of a 50 nm-pore is almost isotropic, very similar to the Rayleigh scattering pattern, and it is irrelevant to different wavelengths. For the 250 nm-pore, the SPD shows a stronger forward scattering pattern, which behaves more evidently at short wavelengths. With the pore diameter increasing to 500 nm, the forward-scattering ratio is further increased with a weakening backward scattering. When the pore diameter equals to 1 μm, there exist multilobes in the SPD, namely, alternate maxima and minima in the SPD.

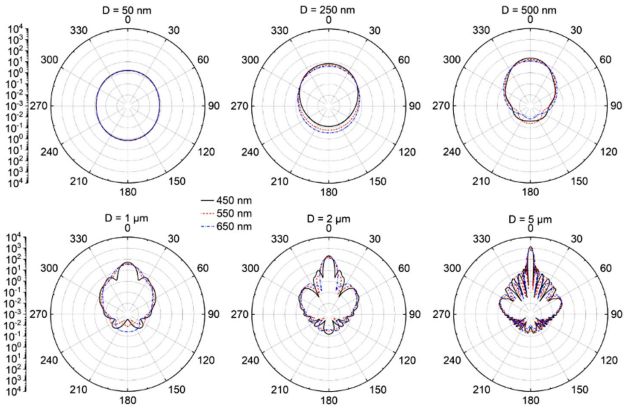

Fig. 7. SPDs of a single spherical pore with different diameters ($D = 50$ nm, 250 nm, 500 nm, 1 μm, 2 μm, 5 μm) embedded in PMMA medium (incident light, unpolarized plane waves with three wavelengths of 450, 550, and 650 nm).

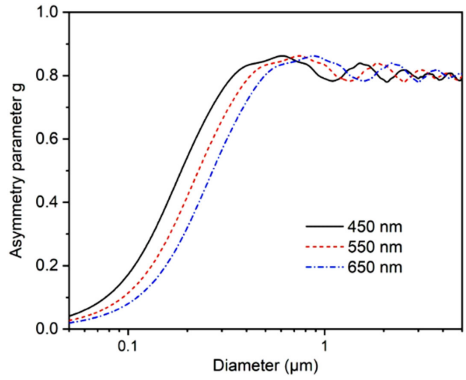

Fig. 8. Asymmetry parameter g of a single spherical pore with different diameters (incident light, unpolarized plane waves with three wavelengths of 450, 550, and 650 nm).

With the further increasing of pore diameter, the number of lobes also increases, and the scattered intensity is more intense at 0°, meaning a dominant forward-scattering mode.

Furthermore, the size- and wavelength-dependent asymmetry parameter g is shown in Fig. 8. The parameter g increases when the pore size is larger and attains a peak at ~1 μm. This variation trend corresponds well with the SPD change. The SPD is nearly isotropic at 50 nm, with a corresponding g value close to 0, and then becomes more forward-scattering-dominant (with g value increasing and eventually going asymptotically to ~ 0.8 with a decaying oscillation).

B. Scattering Analysis of Pore Assembly

Indeed, the foamed porous PMMA film, a mixture of PMMA matrix and numerous pores, forms the pore assembly. Therefore, it is very important to study the scattering property of the pore assembly. The scattering ability of the pore assembly depends on the pore size and number density. Figure 9 shows the relationship between the scattering coefficient of porous film and pore density. Based on the linear superposition, it is not surprising that the scattering coefficient is linearly proportional to the

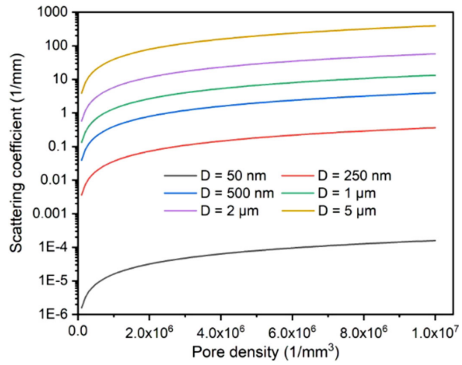

Fig. 9. Relationship between scattering coefficient of porous film with several pore diameters ($D = 50$ nm, 250 nm, 500 nm, 1 μm, 2 μm, 5 μm) and pore number density (incident light, unpolarized plane wave with the wavelength of 450 nm).

number density. Additionally, one can note that the scattering coefficient of the pore assembly is larger when the pore size is larger, which can be compared by the scattering coefficients at a fixed pore number density. Therefore, one should select porous films with a larger pore size if a higher scattering coefficient is required for a given pore number density.

It is worth noting that the above comparison of pore size is based on the same pore number density. However, the volume and thickness of pore assembly is larger when a larger pore size is adopted. From a practical perspective, obtaining the maximum scattering ability at a minimum material use or a constant thickness (volume) is more valuable. The scattering coefficient of porous films at different pore filling fractions is shown in Fig. 10(a). The scattering coefficient is proportional to the filling fraction, as expected, since a higher filling fraction means a larger pore number density. Intriguingly, the scattering coefficient of the 5 μm pore assembly is not the largest one. Indeed, it is just slightly larger than that of the 50 nm pore assembly. Among several pore sizes, the 500 nm pore assembly has the largest scattering coefficient. To illustrate the mechanism underpinning the scattering coefficient difference, the abscissa of Fig. 10(a) is replaced with the pore number density; the relationship is shown in Fig. 10(b). It is shown that the number density is smaller when the pore size is larger at a fixed pore filling fraction. Though the 5 μm pore has the largest scattering cross section, the scattering coefficient of the pore assembly is still small due

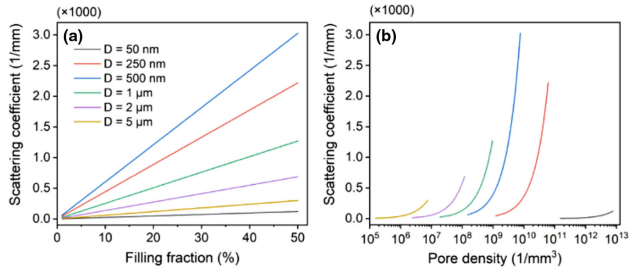

Fig. 10. (a) Relationship between scattering coefficient and pore filling fraction of porous film with several pore diameters ($D = 50$ nm, 250 nm, 500 nm, 1 μm, 2 μm, 5 μm); (b) relationship between scattering coefficient and pore density of porous film [corresponding to the filling fraction in subfigure (a)] (incident light, unpolarized plane wave with a wavelength of 450 nm).

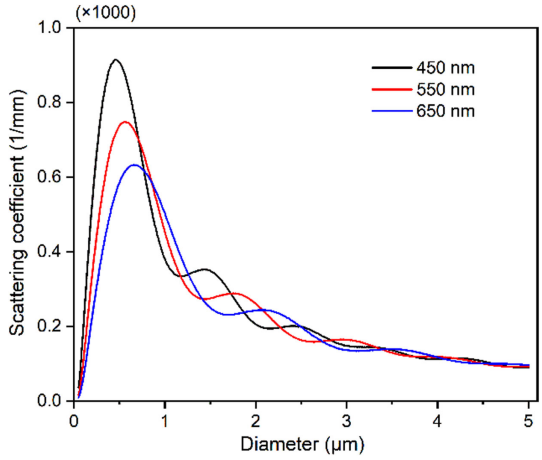

Fig. 11. Relationship between scattering coefficient of porous film and pore diameter under a fill fraction of 15% (incident light, unpolarized plane waves with the wavelength of 450, 550, and 650 nm).

to the limited pore density, and vice versa, for the 50 nm pore assembly. Therefore, both scattering cross section and pore density need to be considered when comparing the scattering coefficient of porous films at a fixed pore filling fraction.

It is of interest to make sure the pore size under which the pore assembly occurs has the maximum scattering coefficient. Hence, we calculate the size-dependent scattering coefficients at a fixed filling fraction 15% (incident light wavelength: 450, 550, 650 nm), as shown in Fig. 11. It is observed that a maximum is always achieved for different incident light wavelengths. For the 450 nm light, the pore assembly attains the maximum scattering coefficient at a pore diameter of ~460 nm. For long-wavelength light, the expected diameter is redshifted. Therefore, it is a good choice to target a pore assembly with wavelength-scale pores for making highly scattering porous films. The results are also in a good agreement with a previous publication [15].

C. Scattering Analysis of Porous Films Made by Microcellular Foaming

To make a detailed analysis about real porous PMMA films, we first fabricated two configurations and obtained their related pore parameters, shown in Fig. 12. Both porous films were foamed under the same processing condition (50 MPa at 80°C). The key for generating different pore sizes is to use PMMA materials with different molecular weights. The PMMA used for foaming micropores has a weight-average molecular weight of 15 K, while the one used for making nanopores features a much higher molecular weight (950 K). It is confirmed that the high-molecular-weight PMMA film has a denser pore distribution and smaller pore size, which is caused by a much higher pore nucleation rate. It has been demonstrated that the exclusion of a low-molecular-weight polymer part can significantly enhance the pore nucleation rate by reducing the nucleation energy barrier [30]. The micropores shown in Fig. 12(a) have a microscale diameter of ~2 μm, much larger than the nanopores with a wavelength-scale diameter of ~400 nm, shown in Fig. 12(b). One should note that the pore number density of nanopore film is 2 orders higher than that of micropore film.

To make an optical simulation for both micropore and nanopore films, the scattering cross sections, scattering coefficients, and asymmetry parameters were calculated based on Mie theory. It is expected that the micropore has a larger scattering cross section than does the nanopore due to the larger geometric size of the micropore. With a much higher pore density, the nanopore film exhibits a larger scattering coefficient than the micropore film. In addition, the asymmetry parameters of both micropores and nanopores are similar. Then the above calculated parameters were used as the input parameters in the ray-tracing simulation. In the simulation, the transmittance values at three typical wavelengths (450, 550, 650 nm) were obtained and compared with the real transmittance. It is shown in Figs. 13(a) and 13(b) that the simulated transmittance values are in a good agreement with the measured transmittance distributions. The transmittance of micropore films is almost unvaried with the wavelength, while the transmittance distributions of nanopore films show a slight wavelength dependency, confirmed by the experiment and simulation results. To make a detailed comparison of micropore and nanopore films, the transmittance versus layer thickness is shown in Fig. 13(c). With a similar thickness of porous layer, the transmittance of nanopore film is smaller than that of micropore film. Note that the PMMA materials for making porous films feature negligible absorption over the visible wavelength range 400–700 nm, which is one of the reasons why PMMA is termed as "organic glass." When light is incident on the porous film, it is either transmitted or reflected. In the scattering process, part of the incident light is forward-scattered, whereas the rest of the energy of the incident light is backscattered (reflected). Therefore, the nanopore films feature a larger reflectivity than the micropore films at a similar thickness, indicating that the scattering ability of nanopore films is stronger than that of micropore films. The comparison results are matched with the scattering coefficient calculation. Therefore, porous films with nanopores should be made to obtain highly scattering ability, which is relevant to real applications demanding a thin system and material saving. To further evaluate the transmission results, we measured the angular transmitted light intensity profiles when 650 nm light was normally incident on the porous films, which are shown in Fig. 14. All the angular intensity profiles show broad angular distributions, confirming the scattering effect caused by the micro- or nanopores introduced inside the porous films. Further, it is noted that with the increasing of film thickness, the intensity at 0°C corresponding to ballistic transmission decreases gradually, whereas the intensity at large angles is enhanced slightly, stemming from more intense scattering. In addition, the overall sum of intensity is reduced with the increasing of film thickness for both micropore and nanopore films, in a good agreement with the transmittance results in Fig. 13.

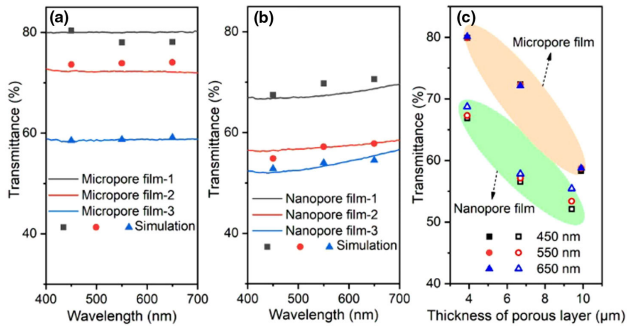

Fig. 13. Measured and simulation transmittance of (a) micropore films (thickness of porous layer: 4, 7, 10 μm for micropore film-1, -2, -3) [24] and of (b) nanopore films (thickness of porous layer: 4, 7, 9 μm for nanopore film-1, -2, -3); (c) measured transmittance of micropore and nanopore films with different thicknesses.

D. Mechanism Analysis of Pores-Enhanced PL in QD Films

To reveal the mechanism of pores-enhanced PL in QD films, a ray-tracing model of 7 μm-thick nanopore film was constructed and simulated in which a fluorescence model was included. The absorption coefficient and PL QY of QD film were set as 4.23 mm^{-1} and 0.5, respectively, which correspond to 1 wt% CdSe/ZnS core-shell QD concentration in the hybrid PMMA-QD film. The incident blue power was set as 1 W. As shown in Fig. 15, the ratios of PL power to the incident power for

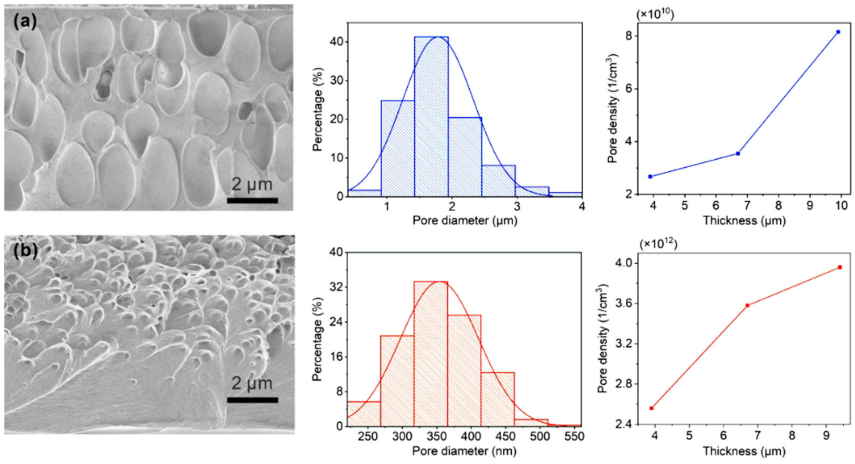

Fig. 12. (a) Micropore film and (b) nanopore film made by microcellular foaming and their pore parameters. Left, SEM images of the cross-sectional morphology; middle, pore diameter distributions; and right, pore density for films with different thicknesses.

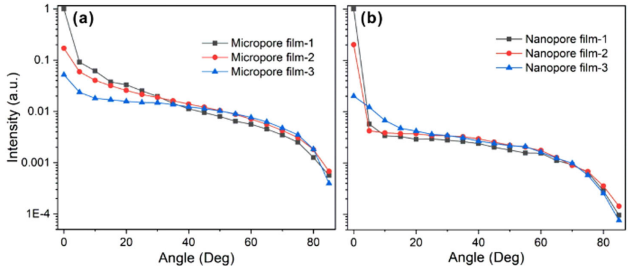

Fig. 14. Normalized far-field angular transmitted intensity distributions of 650 nm incident light impinging on the porous films (data from 0–85° was shown). (a) Micropore films [24], and (b) nanopore films shown in Fig. 13.

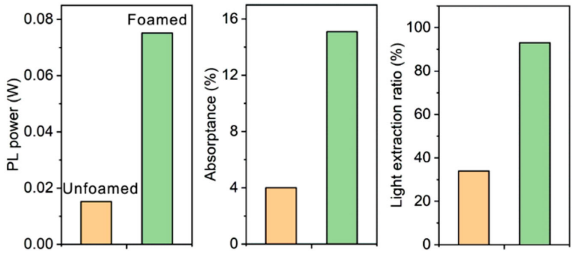

Fig. 15. PL properties of unfoamed and foamed PMMA films (porous layer thickness, 7 μm) obtained in the ray-tracing simulation. Left, PL power; middle, absorptance of excitation light; right, light extraction ratio from the front surfaces for QD emission.

unfoamed and foamed QD films are 1.5% and 7.5%, respectively. The PL intensity of QD film is enhanced by ∼4 times with the assistance of nanopores, which is mainly due to the absorptance enhancement of excitation light, shown in the middle panel of Fig. 15. In addition, the light extraction from front surfaces is of interest to us since it belongs to useful emission in the display and lighting application. Therefore, we show the light extraction ratio from the front surfaces in the right panel of Fig. 15, where a significant enhancement of light extraction ratio is confirmed upon the introduction of porous structures. The reason is that part of the trapped QD emission beyond the total reflection angle interacts with the introduced pores and is extracted to free space by the scattering scheme. The simulation results explain the experimental observation in the previous work well [24].

4. CONCLUSIONS

In this paper, the scattering property of porous films via supercritical CO_2 microcellular foaming was investigated by using Mie scattering theory and ray-tracing simulation. First, a single pore with a diameter much smaller than a wavelength has a dipole-like scattering pattern, whereas the polarization-dependent scattering property is reduced with a larger size of pore. When the pore size is larger, the single pore has a larger scattering cross section. The scattering efficiency and asymmetry factor of the single pore increase with the increasing size and reach peaks of ∼2 and ∼0.8 at a diameter of ∼1 μm, respectively. The above parameters usually have larger values at a shorter wavelength in the wavelength scale or subwavelength range, indicating that pores scatter short-wavelength light more efficiently. As regards pore assembly, the scattering coefficient increases with the increasing pore size, number density, and filling fraction. When the pore filling fraction is fixed, pore assembly with a wavelength-scale pore size has the maximum scattering coefficient, which is relevant with the incident light wavelength. This is due to an optimized combination of scattering cross section and number pore density. Two porous films with micropores and nanopores were made and used for ray-tracing simulation. The simulation results confirmed the validity of the models and demonstrated that nanopore films have stronger scattering ability, in good agreement with the measured transmittance results. The angular light intensity profiles further demonstrated the transmittance difference among various porous films. Lastly, ray tracing with a combined fluorescence model was conducted to illustrate the mechanism of scattering-enhanced PL in QD films. Results showed that pores-induced scattering enhanced the absorption of impinging light and assisted the extraction of trapped QD emission. We believe our work can contribute to the understanding of the scattering ability of foamed porous structures and boost their further application in other similar fields, such as solar cells and radiative cooling.

Funding. National Natural Science Foundation of China (51735004, 51775199); Natural Science Foundation of Guangdong Province (2014A030312017, 2018B030306008); STU Scientific Research Foundation for Talents (NTF19045); Deutsche Forschungsgemeinschaft (DFG, German Research Foundation) (SPP 1839); Germany's Excellence Strategy via the Excellence Cluster 3D Matter Made to Order (EXC-2082/1-390761711).

Acknowledgment. The foaming experiments were carried out at KIT. We gratefully acknowledge kind support from Siegbert Johnsen and Gabriele Wiegand (IKFT, KIT) for the preparation of the foamed samples. We thank Dominik Theobald, Hendrik Hölscher, Uli Lemmer and Guillaume Gomard for stimulating discussions (all KIT). In addition, we are grateful to Guillaume Gomard for his help during the SEM characterization of the samples shown in Figs. 2 and 12. S. Y. acknowledges support from Ms. Dong Fang.

Disclosures. The authors declare no conflicts of interest.

REFERENCES

1. G. Buxbaum, *Industrial Inorganic Pigments* (Wiley, 2008).
2. T. Li, Y. Zhai, S. He, W. Gan, Z. Wei, M. Heidarinejad, D. Dalgo, R. Mi, X. Zhao, J. Song, J. Dai, C. Chen, A. Aili, A. Vellore, A. Martini, R. Yang, J. Srebric, X. Yin, and L. Hu, "A radiative cooling structural material," Science **364**, 760–763 (2019).
3. J. Mandal, Y. Fu, A. C. Overvig, M. Jia, K. Sun, N. N. Shi, H. Zhou, X. Xiao, N. Yu, and Y. Yang, "Hierarchically porous polymer coatings for highly efficient passive daytime radiative cooling," Science **362**, 315–319 (2018).
4. P.-C. Hsu, A. Y. Song, P. B. Catrysse, C. Liu, Y. Peng, J. Xie, S. Fan, and Y. Cui, "Radiative human body cooling by nanoporous polyethylene textile," Science **353**, 1019–1023 (2016).

5. Z. Tang, A. Elfwing, J. Bergqvist, W. Tress, and O. Inganäs, "Light trapping with dielectric scatterers in single-and tandem-junction organic solar cells," Adv. Energy Mater. **3**, 1606–1613 (2013).
6. Z. Li, C. Song, J. Li, G. Liang, L. Rao, S. Yu, X. Ding, Y. Tang, B. Yu, J. Ou, U. Lemmer, and G. Gomard, "Highly efficient and water-stable lead halide perovskite quantum dots using superhydrophobic aerogel inorganic matrix for white light-emitting diodes," Adv. Mater. Technol. **5**, 1900941 (2020).
7. Z.-T. Li, K. Cao, J.-S. Li, Y. Tang, L. Xu, X.-R. Ding, and B.-H. Yu, "Investigation of light-extraction mechanisms of multiscale patterned arrays with rough morphology for GaN-based thin-film LEDs," IEEE Access **7**, 73890–73898 (2019).
8. J. Syurik, R. H. Siddique, A. Dollmann, G. Gomard, M. Schneider, M. Worgull, G. Wiegand, and H. Hölscher, "Bio-inspired, large scale, highly-scattering films for nanoparticle-alternative white surfaces," Sci. Rep. **7**, 46637 (2017).
9. S. Caixeiro, M. Peruzzo, O. D. Onelli, S. Vignolini, and R. Sapienza, "Disordered cellulose-based nanostructures for enhanced light scattering," ACS Appl. Mater. Interface **9**, 7885–7890 (2017).
10. S. Yu, J. Chen, G. Liang, X. Ding, Y. Tang, and Z. Li, "White hairy layer on the *Boehmeria nivea* leaf–inspiration for reflective coatings," Bioinspir. Biomim. **15**, 016003 (2020).
11. S. Tadepalli, J. M. Slocik, M. K. Gupta, R. R. Naik, and S. Singamaneni, "Bio-optics and bio-inspired optical materials," Chem. Rev. **117**, 12705–12763 (2017).
12. W. Barthlott, M. Mail, B. Bhushan, and K. Koch, "Plant surfaces: structures and functions for biomimetic innovations," Nano-Micro Lett. **9**, 23 (2017).
13. P. Vukusic, B. Hallam, and J. Noyes, "Brilliant whiteness in ultrathin beetle scales," Science **315**, 348 (2007).
14. M. Burresi, L. Cortese, L. Pattelli, M. Kolle, P. Vukusic, D. S. Wiersma, U. Steiner, and S. Vignolini, "Bright-white beetle scales optimise multiple scattering of light," Sci. Rep. **4**, 6075 (2014).
15. S. M. Luke, B. T. Hallam, and P. Vukusic, "Structural optimization for broadband scattering in several ultra-thin white beetle scales," Appl. Opt. **49**, 4246–4254 (2010).
16. F. Zeighami and M. A. Tehran, "Developing optically efficient nanofiber coatings inspired by Cyphochilus white beetle," J. Ind. Text. **46**, 495–509 (2015).
17. Y. Tang, Z. Li, G. Liang, Z. Li, J. Li, and B. Yu, "Enhancement of luminous efficacy for LED lamps by introducing polyacrylonitrile electrospinning nanofiber film," Opt. Express **26**, 27716–27725 (2018).
18. Y. Tang, G. Liang, J. Chen, S. Yu, Z. Li, L. Rao, and B. Yu, "Highly reflective nanofiber films based on electrospinning and their application on color uniformity and luminous efficacy improvement of white light-emitting diodes," Opt. Express **25**, 20598–20611 (2017).
19. J. Syurik, G. Jacucci, O. D. Onelli, H. Hölscher, and S. Vignolini, "Bio-inspired highly scattering networks via polymer phase separation," Adv. Funct. Mater. **28**, 1706901 (2018).
20. W. Zou, L. Pattelli, J. Guo, S. Yang, M. Yang, N. Zhao, J. Xu, and D. S. Wiersma, "Biomimetic polymer film with brilliant brightness using a one-step water vapor-induced phase separation method," Adv. Funct. Mater. **29**, 1808885 (2019).
21. H. Go, E.-M. Han, M. H. Kang, Y. H. Kim, and C. Yun, "Fine control of optical scattering characteristics of porous polymer light-extraction layer for organic light-emitting diodes," Org. Electron. **67**, 79–88 (2019).
22. M. S. Toivonen, O. D. Onelli, G. Jacucci, V. Lovikka, O. J. Rojas, O. Ikkala, and S. Vignolini, "Anomalous-diffusion-assisted brightness in white cellulose nanofibril membranes," Adv. Mater. **30**, 1704050 (2018).
23. Z. Fang, H. Zhu, Y. Yuan, D. Ha, S. Zhu, C. Preston, Q. Chen, Y. Li, X. Han, S. Lee, G. Chen, T. Li, J. Munday, J. Huang, and L. Hu, "Novel nanostructured paper with ultrahigh transparency and ultrahigh haze for solar cells," Nano Lett. **14**, 765–773 (2014).
24. S. Yu, B. Fritz, S. Johnsen, D. Busko, B. S. Richards, M. Hippler, G. Wiegand, Y. Tang, Z. Li, U. Lemmer, H. Hölscher, and G. Gomard, "Enhanced photoluminescence in quantum dots–porous polymer hybrid films fabricated by microcellular foaming," Adv. Opt. Mater. **7**, 1900223 (2019).
25. C. F. Bohren and D. R. Huffman, *Absorption and Scattering of Light by Small Particles* (Wiley, 2008).
26. Z. Liu, S. Liu, K. Wang, and X. Luo, "Measurement and numerical studies of optical properties of YAG:Ce phosphor for white light-emitting diode packaging," Appl. Opt. **49**, 247–257 (2010).
27. Z.-T. Li, C.-J. Song, Z.-Y. Qiu, J.-S. Li, K. Cao, X.-R. Ding, and Y. Tang, "Study on the thermal and optical performance of quantum dot white light-emitting diodes using metal-based inverted packaging structure," IEEE Trans. Electron. Devices **66**, 3020–3027 (2019).
28. A. R. Jones, "Light scattering for particle characterization," Prog. Energ. Combust. **25**, 1–53 (1999).
29. J. A. Lock and L. Yang, "Interference between diffraction and transmission in the Mie extinction efficiency," J. Opt. Soc. Am. A **8**, 1132–1134 (1991).
30. C. M. Stafford, T. P. Russell, and T. J. McCarthy, "Expansion of polystyrene using supercritical carbon dioxide: effects of molecular weight, polydispersity, and low molecular weight components," Macromolecules **32**, 7610–7616 (1999).